GALAXY CLUSTERS AT THE EDGE: TEMPERATURE, ENTROPY, AND GAS DYNAMICS NEAR THE VIRIAL RADIUS

JACK O. BURNS[1], SAMUEL W. SKILLMAN[1,3], AND BRIAN W. O'SHEA[2]
[1] Center for Astrophysics and Space Astronomy, Department of Astrophysical and Planetary Science, University of Colorado, Boulder, CO 80309, USA;
jack.burns@cu.edu
[2] Department of Physics and Astronomy and Lyman Briggs College, Michigan State University, East Lansing, MI 48824, USA

ABSTRACT

Recently, *Suzaku* has produced temperature and entropy profiles, along with profiles of gas density, gas fraction, and mass, for multiple galaxy clusters out to approximately the virial radius. In this paper, we compare these novel X-ray observations with results from *N*-body + hydrodynamic adaptive mesh refinement cosmological simulations using the *Enzo* code. There is excellent agreement in the temperature, density, and entropy profiles between a sample of 24 mostly substructure-free massive clusters in the simulated volume and the observed clusters. This supports our previous contention that clusters have "universal" outer temperature profiles. Furthermore, it appears that the simplest adiabatic gas physics used in these *Enzo* simulations is adequate to model the outer regions of these clusters without other mechanisms (e.g., non-gravitational heating, cooling, magnetic fields, or cosmic rays). However, the outskirts of these clusters are not in hydrostatic equilibrium. There is significant bulk flow and turbulence in the outer intracluster medium created by accretion from filaments. Thus, the gas is not fully supported by thermal pressure. The implications for mass estimation from X-ray data are discussed.

Key words: cosmology: observations – cosmology: theory – hydrodynamics – intergalactic medium – methods: numerical – X-rays: galaxies: clusters

1. INTRODUCTION

Galaxy clusters are unique and potentially powerful cosmological probes of the universe. They are the largest gravitationally bound objects, having grown hierarchically within the large-scale cosmic web. As such, clusters are an important source of information about the components of the universe in which they formed and evolved (e.g., Voit 2005; Borgani & Kravtsov 2009). Gravity drives structure formation within an expanding universe, with regions of density higher than the average becoming gravitationally bound and decoupling from the expansion. Clusters probe the high-density tail of this cosmic density field. The number density of clusters is strongly dependent upon the specific cosmological model, especially when viewed as a function of redshift (e.g., Rosati et al. 2002). The mass function of clusters and its evolution are also sensitive to σ_8 (a parameter that quantifies the rms density fluctuations on comoving scales of 8 h^{-1} Mpc). The potential to use the cluster mass function to measure cosmological parameters is challenging observationally because mass is not a direct observational quantity. Rather, X-ray luminosity, X-ray temperature (e.g., Henry et al. 2009), thermal Sunyaev–Zeldovich effect (SZE), integrated Compton-y parameter $Y (\propto \int \rho T \, dl \, dA$; e.g., Motl et al. 2005), or weak lensing shear (e.g., Oguri et al. 2010) are the observables which must then be translated into an estimate of cluster mass.

Over the past decade, X-ray observations from *ROSAT*, *Chandra*, *XMM-Newton*, and, more recently *Suzaku*, have begun to produce significant samples of clusters out to $z \approx 1.3$ (e.g., Allen et al. 2008). With these samples, it is becoming possible to distinguish between cosmological models using the evolution of the cluster mass function (e.g., Vikhlinin et al. 2009) and the cluster gas fraction (e.g., Rapetti et al. 2008). The primary limiting factor in such applications remains accurate conversion between observables such as X-ray luminosity and

temperature to cluster mass. This is complicated by the nonlinear baryonic processes at the cores of clusters, including radiative cooling, thermal conduction, and non-gravitational heating from supernovae and active galactic nuclei (AGNs; e.g., Ruszkowski & Begelman 2002; Heinz et al. 1998; Burns 1998), and possibly nonthermal processes involving cosmic rays (e.g., see Skillman et al. 2008) and magnetic fields (e.g., see Churazov et al. 2008; Xu et al. 2009). Other complications include possible bias and scatter in scaling relations (Motl et al. 2005; Nagai 2006), as well as errors created by assuming that cluster gas is in hydrostatic equilibrium (e.g., see Lau et al. 2009; Burns et al. 2008; Rasia et al. 2006; Nagai et al. 2007).

The outer extremities of galaxy clusters are expected to differ markedly from the cores. The peripheries of clusters have lower gas and galaxy densities, and long cooling times comparable to the Hubble time, thus potentially making the thermodynamics simpler than in the cores. At the same time, the outer regions of clusters are closer to the sources of accretion from filaments and, therefore, the gas dynamics may be more complex. In this paper, we explore the properties of clusters near the virial radius by comparing cosmological numerical simulations with observations.

The intracluster gas in galaxy clusters is often assumed to be in hydrostatic equilibrium, which relates the gravitational potential (Φ) to the gas pressure (P) and the gas density (ρ) such that

$$\nabla \Phi = -\frac{\nabla P}{\rho}. \tag{1}$$

Applying Gauss's law to the gravitational potential in the above equation, the cumulative mass is

$$M(<r) = \frac{1}{4\pi G} \int -\frac{\nabla P}{\rho} dA, \tag{2}$$

where G is Newton's gravitational constant and the integral is over a spherical surface area with radius r. If the cluster is

---

further assumed to be spherically symmetric and the pressure arises only from thermal motions ($P = \rho k T / [\mu m_p]$), then

$$M(< r) = -\frac{r^2 k}{\rho G \mu m_p} \left[T \frac{d\rho}{dr} + \rho \frac{dT}{dr} \right]. \qquad (3)$$

As seen in Equation (3), it is necessary to measure both the gas densities and temperatures, along with their gradients, to calculate the hydrostatic equilibrium masses. Gas density profiles can be accurately determined from the X-ray surface brightness, S_X, since $S_X \propto \rho^2$ with only a weak dependence on temperature.

Temperature profiles, on the other hand, are more challenging since they require spatially resolved X-ray spectroscopic observations acquired from relatively long integrations. This proves to be difficult, particularly to measure cluster temperatures beyond $\sim 0.5 r_{200}$.[4] Because of the low and stable particle background levels at its orbit, *Suzaku* has begun to change the landscape by producing temperature profiles out to $\approx r_{200}$ for a small number of clusters including PKS 0745−171 (George et al. 2009), A1795 (Bautz et al. 2009), A399/401 (Fujita et al. 2008), A1689 (Kawaharada et al. 2010), A2204 (Reiprich et al. 2009), and A1413 (Hoshino et al. 2010). In each cluster, the temperature is observed to decline by a factor of ≈ 3 from the peak near the cluster core to regions at $\approx r_{200}$.

Using the Eulerian adaptive mesh refinement (AMR) cosmology code *Enzo* for a ΛCDM universe, our group first proposed a universal temperature profile for galaxy clusters (Loken et al. 2002). This average profile was well fit by a power law out to the virial radius. We did not find any significant difference in the outer temperature profiles for simulations with simple adiabatic gas physics or more complex models with cooling and star formation. Furthermore, this profile agreed well with the X-ray data available at that time for nearby clusters from *BeppoSAX* (De Grandi & Molendi 2002). Subsequent *Chandra* observations also appear consistent with such a universal temperature profile beyond the dense central cores for galaxy clusters (e.g., Vikhlinin et al. 2006). However, these observed temperature profiles extended out only to $\approx 0.5 r_{200}$, so it was unclear if the universal temperature profiles for numerical clusters are in agreement with the outer profiles for real clusters.

In this paper, we compare the temperature, density, and entropy profiles for a new sample of numerical clusters generated using the *Enzo* cosmology code with new observations from *Suzaku*. We ask the question: do real clusters follow a universal temperature profile out to the virial radius, as is predicted by numerical simulations with simple adiabatic gas physics? We also explore the implications of this particular form of the universal temperature profile for hydrostatic equilibrium, intracluster gas dynamics generated by ongoing accretion in the outer periphery of clusters, and cluster mass estimation.

In Section 2, we describe the *Enzo* cosmology code and the numerical simulations used for the comparison with X-ray observations. In Section 3, we compare gas densities, temperatures, and entropy profiles between our numerical simulations and observed clusters. Then, in Section 4, we explore the implications of the form of the observed and simulated cluster temperature profiles on hydrostatic equilibrium and cluster mass determinations. We end with a summary and conclusions in Section 5.

---

[4]　r_{200} is the radius enclosing an overdensity $\Delta_{200} = 200\rho_{\rm crit}$, where $\rho_{\rm crit}(z) = 3H(z)^3/(8\pi G)$ is the critical density. For a concordance ΛCDM universe, $\Delta_c \approx 178\Omega_M^{0.45} \approx 100$, where Δ_c is the overdensity that encloses the virial mass (Eke et al. 1998). Using the scaling relation for $\rho_{\rm DM}/\rho_{\rm crit}$ in Equation (3) of Eke et al. (1998), $r_{200} \approx 0.77 r_{100}$.

Table 1
Comparison of Properties of Simulated with Observed Clusters

| Cluster	z	M_{200} ($M_\odot$)	r_{200} (Mpc)
PKS 0745−191	0.103	6.4×10^{14}	1.72
A1795	0.063	8.6×10^{14}	1.9
Simulated Clusters	0.05	1.7–10×10^{14}	1.6–2.8

2. SIMULATIONS

We use the *Enzo* AMR *N*-body + hydrodynamics cosmology code (Bryan & Norman 1997a, 1997b; Norman & Bryan 1999; O'Shea et al. 2004; O'Shea et al. 2005) to simulate a comoving volume of $(128\,h^{-1}$ Mpc$)^3$ with 256^3 root-grid cells and up to five levels of additional refinement. This simulation utilizes the ZEUS finite-difference method (Stone & Norman 1992a, 1992b). The AMR is controlled by refining any region that is overdense by a factor of 8 in either the dark matter or gas density. The peak resolution is $15.6\,h^{-1}$ kpc (comoving). The initial conditions are generated from an Eisenstein & Hu (1999) power spectrum with a primordial spectral index $n_s = 0.97$. We use the cosmological parameters $(h, \Omega_M, \Omega_B, \Omega_\Lambda, \sigma_8) = (0.70, 0.268, 0.0441, 0.732, 0.9)$, with $h = H_0/(100$ km s^{-1} Mpc^{-1}) (Spergel et al. 2007). The simulation was initialized at $z = 99$ and run until $z = 0$. The dark matter mass resolution is $3.12 \times 10^9\,h^{-1}\,M_\odot$. For a further exposition of *Enzo* and its use in studying the statistical properties of clusters, see Skillman et al. (2008, 2010).

3. COMPARISON OF SIMULATED AND OBSERVED CLUSTERS

We used the halo-finding algorithm HOP (Eisenstein & Hut 1998), as implemented in *yt*,[5] to identify clusters in the simulated volume, using the standard set of density thresholds. We then selected the 40 most massive halos in our volume at $z = 0.05$ for comparison with the *Suzaku* observations because these clusters best match those observed (Table 1). The distribution of cluster masses is shown in Figure 1. We note that the modest simulated volume generates a limited dynamic range of masses, from 1.7 to $10 \times 10^{14}\,M_\odot$. In our previous papers reporting on similar simulations (e.g., Jeltema et al. 2008), we did not find any significant variations in such quantities as the ratio of hydrostatic to true mass as a function of mass for a similar mass range as in Figure 1.

This master sample was edited by examining the three-dimensional distribution of the dark matter. If the primary dark matter density peak is located outside of $0.1 r_{200}$ with respect to the center of mass, the cluster is marked as "disturbed" and is removed from the analysis pipeline. This is most prevalent in clusters undergoing mergers where the existence of two or more halos offset the center of mass. Upon visual inspection, these clusters were confirmed to be the ones with major substructure. This produced a "clean" sample of 24 most massive clusters that are relatively relaxed. The full sample is shown in Figure 2, with "disturbed" clusters shown with a red "X" through the density projections. However, a note of caution is warranted, as there is accretion of smaller halos (subclusters) present in nearly all clusters; such small halo accretion is better seen in temperature images where shocks from supersonically merging subclusters are more obvious (see Figure 2).

---

[5]　http://yt.enzotools.org
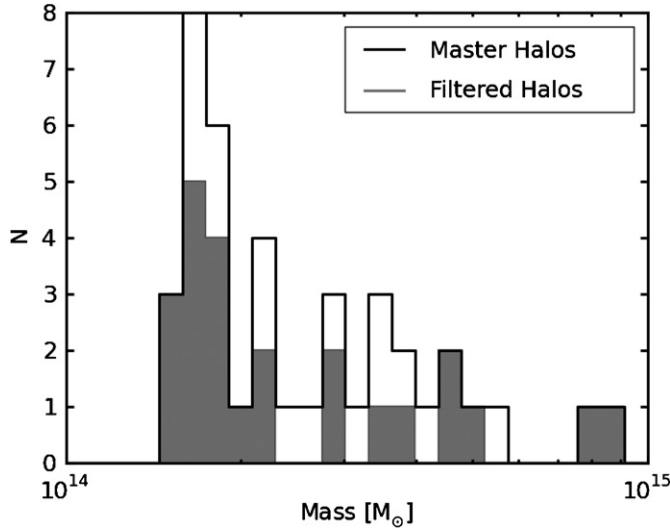
Figure 1. Distribution of galaxy cluster masses from *Enzo* simulations. The master sample contains 40 halos. The filtered halos (24) are the ones in which obvious major mergers have been eliminated (see Figure 2).

A grid of images of gas densities, temperatures, and 0.5–12.0 keV fluxes is portrayed in Figure 2. For each temperature and density projection, we show a corresponding X-ray image. The method of Smith et al. (2008) was used to calculate energy-dependent emission using the emission function from the Cloudy code (Ferland et al. 1998). Given a temperature and density of the gas, and assuming a metallicity of 0.3 $Z_\odot$, this returns the 0.5–12.0 keV emissivity. The flux is the integral along the line of sight of the emissivity. The images in Figure 2 show a good deal of non-circularly symmetric structures, often produced by accretion along filaments, as also appears to be seen in the clusters observed by *Suzaku* (e.g., George et al. 2009; Bautz et al. 2009).

3.1. Analysis Pipeline

3.1.1. Three-dimensional Profiles

For each cluster, we create spherically averaged radial profiles centered on the center of mass of the cluster. We track the following key fields: radius (in Mpc), overdensity of a sphere out to the current radius with respect to the background density ($\Omega_m \rho_{\rm crit}$), dark matter density, gas density, entropy, pressure, specific radial kinetic energy, specific kinetic energy, temperature, thermal energy, X-ray emission, total energy, and enclosed baryonic + dark matter mass.

An important point in our profiling procedure involves various options for weighting the profiles. In this study, we use two different methods. First we can use the simple method of weighting by the mass of the cell. Therefore, regions in radial shells in high-density regions will be weighted higher than those in underdense regions. Second, we weight by the total X-ray emission emanating from each cell. This biases toward overdense regions even more strongly since the X-ray emissivity scales roughly with ρ^2. In Figures 3 and 4, we use X-ray weighting to compare with X-ray observables. In Figure 5, we use mass weighting to investigate the physical causes of deviations from hydrostatic equilibrium.

3.1.2. Profiles of Two-dimensional Projections

Because observations yield inherently two-dimensional images, it is important to compare projections of our clusters to the true observations. We do this by first creating halo projections of each cluster that encompass an 8 Mpc cube around the individual cluster. For each of these projections, we again have a choice between weighting by the density (or mass, $T_{\rm mw}$) or X-ray emission ($T_{\rm ew}$). Unless otherwise noted, we will use only the projections weighted by the X-ray emission. From each of the two-dimensional projections, we then seek to create radial profiles. Here we give details of creating two-dimensional profiles of $T_{\rm ew}$, and use the same technique in all other quantities.

For each cluster, we first make a projection of the X-ray emissivity, ϵ_X, which yields the flux,

$$S_X(x, y) = \int \epsilon_X(x, y, z)dz. \tag{4}$$

We then make a projection of the temperature, weighted by X-ray emissivity,

$$T_{\rm Proj,ew}(x, y) = \frac{\int T(x, y, z)\epsilon_X(x, y, z)dz}{S_X(x, y)}. \tag{5}$$

From these quantities, we create the profiles of the two-dimensional projections by weighting the temperature projection by the surface brightness,

$$T_{\rm 2D,ew}(r) = \frac{\int T_{\rm Proj,ew}(x, y)S_X(x, y)rd\theta}{\int S_X(x, y)rd\theta}, \tag{6}$$

where r and θ are the normal polar coordinates. This results in a correctly weighted radial profile of emission weighted temperature. Note that this is different than simply creating a two-dimensional profile from the projection of emission weighted temperature. We can compare this final step to the equivalent step in the creation of the spherically averaged radial profile of the same quantity using normal spherical coordinates,

$$T_{\rm 3D,ew}(r) = \frac{\int \int T(x, y, z)\epsilon_X(x, y, z)r^2 \sin\theta d\theta d\phi}{\int \int \epsilon_X(x, y, z)r^2 \sin\theta d\theta d\phi}. \tag{7}$$

3.2. Results

Applying the approach described in Section 3.1 to the analysis of the simulated clusters, we produced radial profiles of density, temperature, and entropy as shown in Figure 3. The profiles were constructed by binning in circular annuli centered on the peak emission. For the density and entropy profiles, we show the median values for the numerical clusters; this is very effective in reducing variations due to substructure caused by multiple, small infalling subclusters. The shaded regions illustrate the standard deviations in quantities derived from the sample of numerical clusters. The scatter in the profiles generally grows with radial distance, especially for the density and entropy, beyond $\approx 0.7r_{200}$. This scatter reflects real variations from cluster to cluster in the outer regions produced by non-spherically symmetric accretion along filaments as mentioned above. The density and entropy profiles were normalized to the value at $0.5r_{200}$, a good midway point between the core and the outer cluster region. The temperature profiles were each normalized to their X-ray weighted average values between 0.2 to 1.0 r_{200}.

In Figure 3, we define entropy as $K \equiv kT\left(\frac{\rho}{\mu m_p}\right)^{-2/3}$. The flat outer profile ($>0.5r_{200}$) seen for the median entropy of the numerical cluster sample in Figure 3 is, in part, due to the
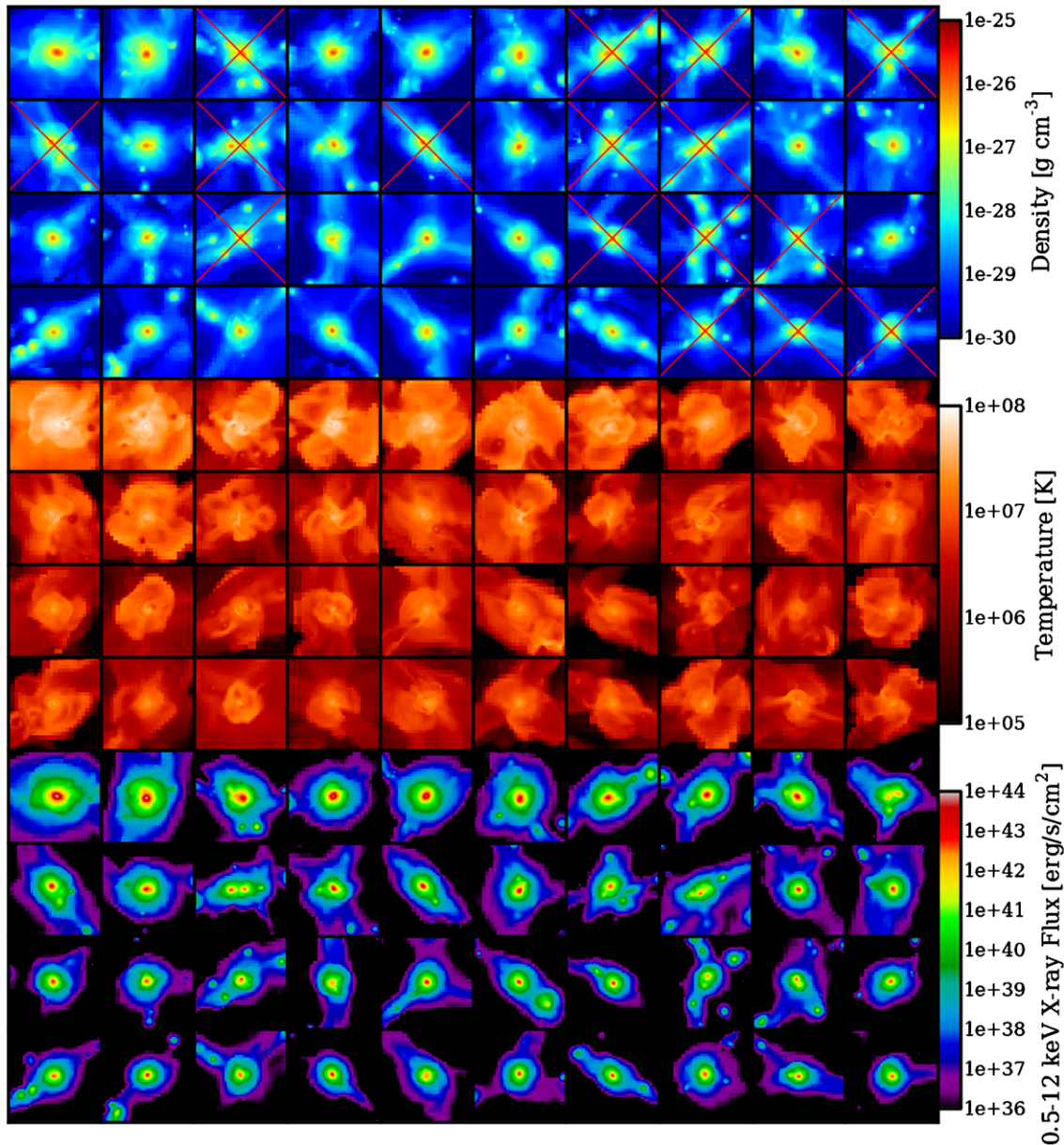
Figure 2. Grid of images of the 40 most massive clusters in the numerical sample selected from a cosmological volume at $z = 0.05$. The images are ordered by M_{200} from the upper left (10^{15} $M_{\odot}$) to the lower right (1.7×10^{14} $M_{\odot}$) for each of the three panels of gas density (top), temperature (middle), and X-ray flux (bottom). Field of view of each image is 8 h^{-1} Mpc. The range of properties for these clusters is listed in Table 1. This sample was reduced to 24 clusters for statistical analysis by eliminating obvious merger systems (marked by the red X on the density image).

averaging of individual profiles, some with positive and some with negative slopes.

The average temperature two-dimensional profile shown in Figure 3 is well fit by a function of the form

$$\frac{T}{T_{\mathrm{avg}}} = A\left[1 + B\left(\frac{r}{r_{200}}\right)\right]^{\alpha}, \qquad (8)$$

where a linear least-squares fit of the parameters A, B, and α without any priors yield $A = 1.74 \pm 0.03$, $B = 0.64 \pm 0.10$, and $\alpha = -3.2 \pm 0.4$. As we discuss in Section 4, the particular shape/slope of this power law for the temperature profile has implications for understanding the gas dynamics and ICM pressure support in the outer regions of clusters.

In Figure 3, we also compare the numerical profiles with the observed ones for two nearby clusters (PKS 0745−191 and

A1795) with recent *Suzaku* measurements that extend out to $\sim r_{200}$. A summary of the characteristics of these two observed clusters, along with the average properties of the numerical clusters, is given in Table 1. Both observed clusters have small cool cores. Since our simulations were purposely constructed with simple adiabatic gas physics, we did not expect to match the central regions of these clusters. Instead, we focus on the outer profiles, beyond $\gtrsim 0.5r_{200}$. Other clusters recently observed by *Suzaku* have similar outer temperature profiles with a factor of ≈ 3 decline in temperature between the core and r_{200} (e.g., Reiprich et al. 2009; Hoshino et al. 2010).

It is clear from this figure that the outer cluster radial distributions of density, temperature, and entropy for PKS 0745−191 and A1795 agree well with the simulated clusters. From Figure 3, we draw two conclusions about the regions outside the cluster cores. First, the observed clusters follow
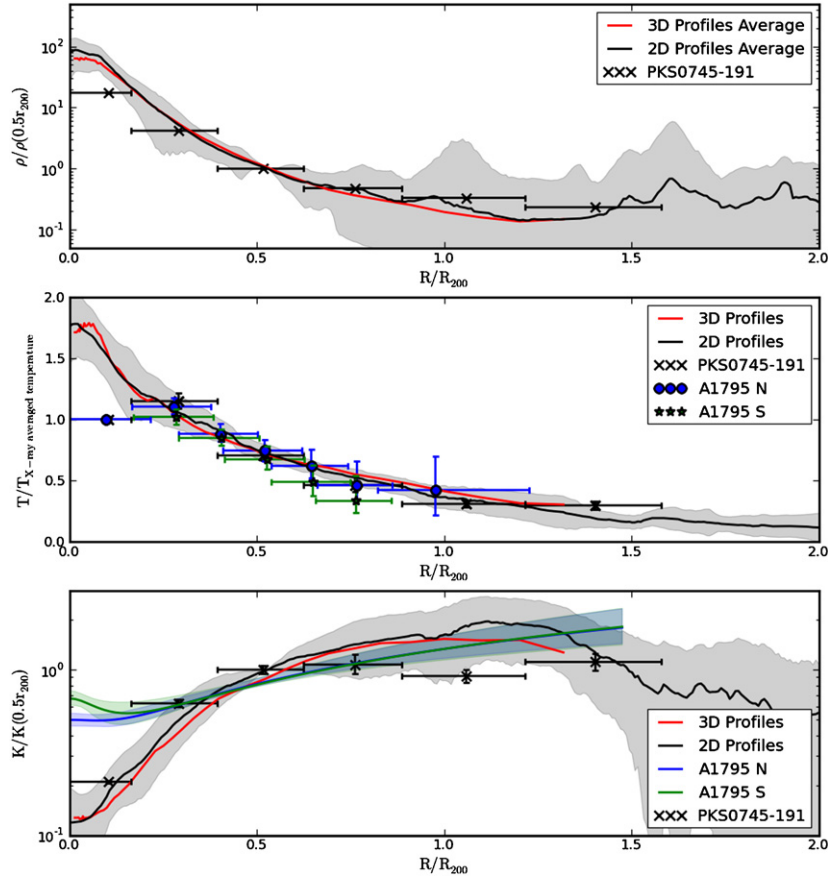
Figure 3. Three- and two-dimensional X-ray weighted average profiles, as described in Section 3.1, of normalized density, temperature, and entropy for simulated clusters. The shaded regions are the standard deviations of each quantity produced from the scatter within the sample of numerical clusters. The *Suzaku* data points for PKS 0745−191 and A1795 (measured for two separate analysis regions, north (N) and south (S) of the core) are shown for comparison. The blue and green shaded regions in the bottom entropy profile are for the N and S analysis regions of A1795. The density and entropy profiles are normalized to their values at $0.5r_{200}$, whereas the temperature profiles are normalized to their X-ray weighted average values between 0.2 and 1.0 r_{200}.

"universal" temperature, density, and entropy profiles as characterized by numerical simulations out to the outer bounds of the clusters (r_{200}).

Second, the simplest intracluster medium (ICM) gas physics with an adiabatic equation of state may be sufficient to characterize the thermodynamic gas properties of the peripheries of these clusters. With the present *Suzaku* data, added gas physics such as radiative cooling, non-gravitational heating via low power AGNs associated with non-central cluster galaxies (e.g., Hart et al. 2009) or nonthermal pressure due to ICM B-fields and cosmic rays (e.g., Skillman et al. 2008) are not required, as also found by Loken et al. (2002) and Roncarelli et al. (2006). Metallicity gradients in the outer regions of clusters are seen in simulations (e.g., Tornatore et al. 2010; Fabjan et al. 2010) and in observations (e.g., Lovisari et al. 2009). The observed self-similarity in the L_X-M scaling relation, revealed when cluster cores are excised (Mantz et al. 2010), may suggest that the metallicity gradients are caused by mixing rather than energy/entropy injection. The effects of higher/lower metallicity in clusters is not well understood so it is not yet clear if deviations from adiabatic physics is necessary.

4. DISCUSSION

4.1. Are Galaxy Clusters in Hydrostatic Equilibrium?

What does the particular shape of the observed and numerical cluster temperature profiles imply about the dynamical state of the ICM? In particular, is this universal temperature profile consistent with the simplest form of hydrostatic equilibrium given in Equation (3), where the ICM pressure is strictly thermal?
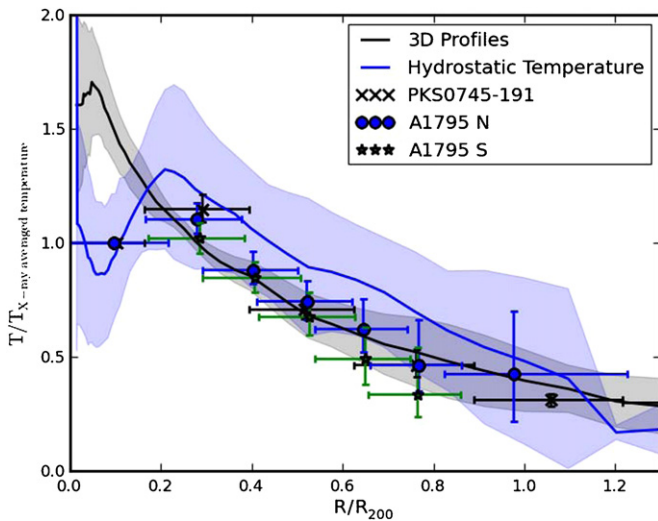
In Figure 4, we compare the temperature profiles from the observed clusters and the simulations with that expected if the numerical clusters are in hydrostatic equilibrium. To calculate the hydrostatic temperature, we begin by making spherically averaged three-dimensional radial profiles of the dark matter density, weighted by the X-ray emission. From these radial profiles, we calculate the total enclosed mass as a function of radius. We then assume hydrostatic equilibrium to calculate the pressure derivative at each point,

$$dP = -\frac{GM(r)(\epsilon\rho_{dm})}{r^2}dr, \qquad (9)$$

where $\epsilon = \rho_{gas}/\rho_{dm}$ is the ratio of gas to dark matter density and is assumed to be constant. We then integrate the pressure inwards, assuming $P = 0$ at our outermost radial point. Finally, we calculate the temperature from

$$T_{hydro} = \frac{\mu m_p P}{k\epsilon\rho_{dm}}. \qquad (10)$$

Because we normalize the temperature, the absolute scaling of the pressure (and the value of ϵ) does not affect the result. From the set of each individual profile, we then calculate the mean and standard deviation shown in Figure 4.

Figure 4. Comparison of numerical and observed cluster temperature profiles with that expected for hydrostatic equilibrium. The blue line and blue shading are the temperature distribution and standard deviations, respectively, expected if the gas in the dark matter potential wells of simulated halos is in hydrostatic equilibrium. The black line and gray shading are the X-ray weighted average temperature and standard deviations, respectively, for the numerical clusters. *Suzaku* data points are also shown for PKS 0745−191 and for two analysis regions (north and south) in A1795.

Using a χ^2 test to compare the temperatures and their standard deviations for the simulated clusters in Figure 4, we find that the numerical three-dimensional radial temperature profile and $T_{hydro}(r)$ have a 1.6% probability of being drawn from the same parent distribution. Although the scatter is large, the average hydrostatic temperature profile is ≈20% higher than the three-dimensional numerical clusters or observed *Suzaku* clusters temperature profiles. This raises concerns about accurately calculating cluster masses using this method, especially for applications to precise cosmological parameter estimation.

In Figure 5, we investigate this issue further by plotting $(M_{hydro}(< r) - M_{true}(< r))/M_{true}(< r)$, where $M_{hydro}(< r)$ is the mass within a sphere with radius r calculated from hydrostatic equilibrium using Equation (3) and $M_{true}(< r)$ is the dark matter mass. In this case, we use a mass weighting to probe the physical cause of the differences in mass. Previous numerical simulations have shown that there is a systematic bias (underestimate) of 5%–15% in the calculated mass of the central to mid regions of clusters ($r_{2500} - r_{500}$) (Burns et al. 2008; Rasia et al. 2006; Lau et al. 2009; Piffaretti & Valdarnini 2008) assuming hydrostatic equilibrium. Figure 5 illustrates that this bias increases towards the edge of clusters. Beyond ≈$0.8r_{200}$, the average integrated mass is biased low by ≈15%. Recent observational work (Mahdavi et al. 2008) as well as other simulations (e.g., Meneghetti et al. 2010) support this result in that hydrostatic cluster mass estimates are found to be systematically low by 5%–20% compared to masses calculated via weak lensing out to r_{500}. Importantly, Figure 5 also illustrates the large scatter in the hydrostatic equilibrium calculation due to different dynamical states of individual clusters (even when applied to clusters not undergoing major mergers, i.e., the sample of 24 clusters in Figure 2). At $0.8r_{200}$, cluster hydrostatic masses range from 5% overestimates to 30% underestimates.

4.2. Gas Dynamics in the Outer Regions of Clusters

Why does the ICM of galaxy clusters not follow the simple prescription for hydrostatic equilibrium shown by Equation (3)?
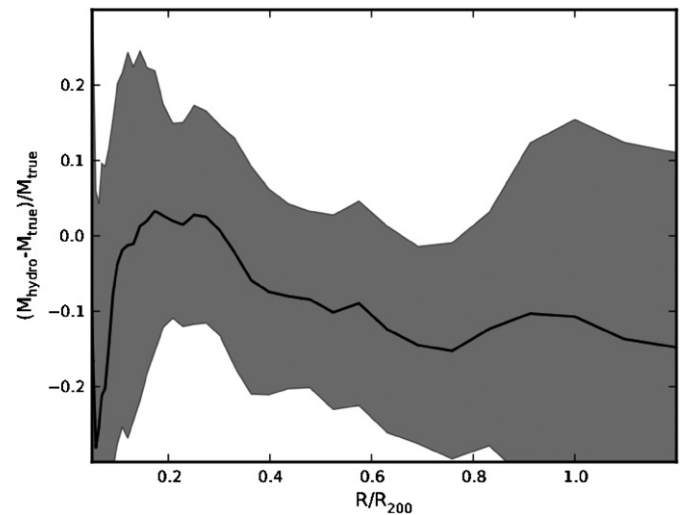
Figure 5. Radial profile of the fractional difference between cluster mass assuming hydrostatic equilibrium and the true mass for the sample of numerical clusters. The shaded region is the standard deviation around the mean values.

There are several obvious reasons which relate to the connection of clusters with the cosmic web and to their ongoing evolution via accretion of gas and subclusters from filaments.

First, unlike the view several decades ago, galaxy clusters are not simple spheres of gas and dark matter that are disconnected from their surroundings. Rather, they are closely tied to linear filaments within the large scale structure of the universe. Gas, galaxies, and dark matter are funneled along these filaments into clusters, which typically lie at the intersections of the filaments. As a result, accretion onto clusters is complex and nonspherical. Thus, azimuthal variations in ∇P using Equation (2) need to be folded into the calculation of $M(< r)$.

Second, this accretion also leads to bulk flows and turbulent gas motions in the ICM. The bulk gas velocities are often hundreds to even thousands of km s^{-1} which may be detectable with upcoming high resolution X-ray calorimeter spectrometers (e.g., Astro-H XCS). One symptom of these bulk velocities and turbulent motions is the complex asymmetric temperature structures which are visible in simulated clusters as shown in Figures 2 and 6. The particular visualization in Figure 6 was chosen to display thin isocontours of temperature, highlighting the various phases of the intracluster gas. This temperature image illustrates the complex interplay between gas of different temperatures (and velocities) accreting from filaments at multiple angles and thermalizing via a web of shocks throughout the cluster.

Third, the kinetic gas motions are a significant fraction of the total energy density of the ICM, especially in the outer reaches of clusters. In Figure 7, we plot the radial profiles of the ratios of the thermal (nkT), radial kinetic (ρv_r^2), and turbulent kinetic energy ($\equiv$ difference between total and radial kinetic energy) densities to that of the total kinetic + thermal energy density of the gas in our numerical clusters. To calculate the kinetic energy density of the gas, we first find the center of mass velocity of the halo. We then compute the difference between a cell's velocity and this center of mass velocity. This then gives the kinetic motion relative to the halo. Both the kinetic energy and thermal energy are calculated using a mass weighting. Near the cluster centers ($\lesssim 0.2r_{200}$), the radial kinetic and turbulent kinetic energies contribute only ≈15% to the total gas energy of the ICM, consistent with mild biasing of the hydrostatic mass
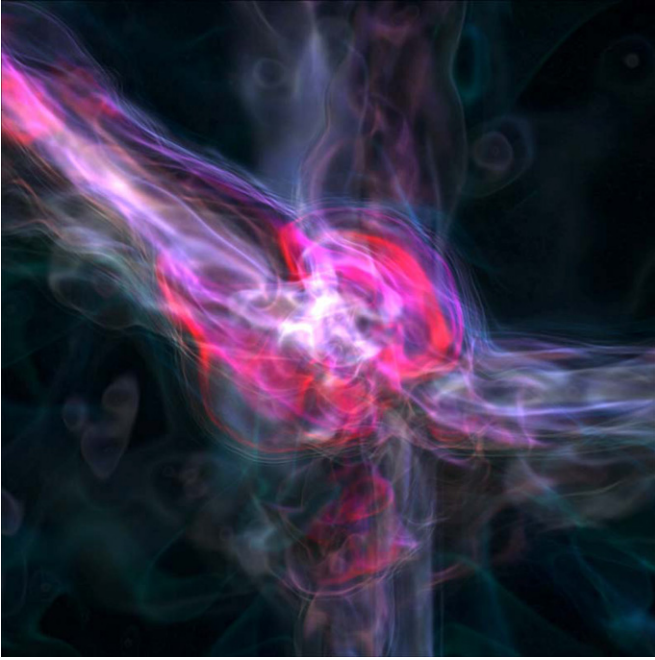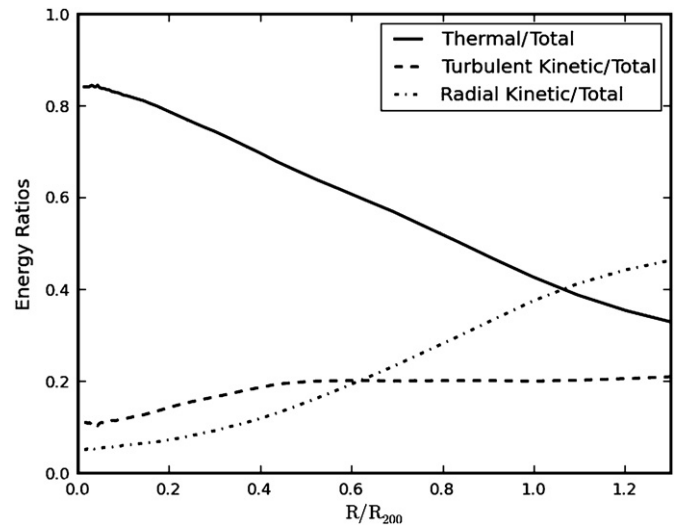
Figure 6. Isocontours of temperature for a numerical cluster. The field of view is 13.85 h^{-1} Mpc. The colors correspond to the following temperatures: cyan = 10^5 K, magenta = 3×10^5 K, blue = 10^6 K, orange = 3×10^6 K, red = 1.6×10^7 K, and white = 5×10^7 K. This new visualization was created using a ray casting module recently developed within *yt*.

Figure 7. Energy density ratio profiles for the sample of numerical clusters. The thermal, radial kinetic, and turbulent kinetic energy densities are normalized to the total gas energy. Total is defined here as total kinetic + thermal energy density within each shell. Turbulent kinetic energy is the total kinetic minus the mean radial kinetic energy.

estimates in the central regions of clusters. However, at r_{200}, the radial kinetic energy equals the thermal energy. Furthermore, the turbulent energy density at the cluster edge is ≈50% of the thermal energy and, thus, provides significant pressure support. So, it is not surprising that hydrostatic equilibrium increasingly fails as a valid assumption as we get closer to the cluster periphery. Turbulent gas motion is an important ingredient in the pressure support of galaxy clusters (see also Vazza et al. 2009). For Equation (2) to result in an accurate estimate of cluster mass, it must contain a dynamical gas pressure term ($\sim \rho v^2$; see also Lau et al. 2009).

5. SUMMARY AND CONCLUSIONS

Suzaku has recently produced exciting new observations of temperatures and entropies for a small sample of galaxy clusters out to ≈r_{200}, near the virial radius. These data reveal similar temperature profiles that decline by a factor of ≈3 between the central regions and r_{200}. We compared these pioneering *Suzaku* observations with synthetic X-ray temperature profiles of clusters constructed from cosmological hydro/*N*-body simulations using the *Enzo* code. These simulations were run with simple adiabatic gas physics since we were most interested in modeling the outer regions of clusters where the cooling times exceed the Hubble time. Using a sample of 24 mostly substructure-free numerical clusters, we compared the density, temperature, and entropy profiles with *Suzaku* observations of two rich galaxy clusters, PKS 0745−191 and A1795. As shown in Figure 3, the agreement between observations and simulations is very good. With the present *Suzaku* data, radiative cooling, non-gravitational heating (via e.g., AGNs), magnetic fields, or cosmic ray pressure effects are not required.

Interestingly, we find that these profiles are not consistent with simple hydrostatic equilibrium in the outer cluster regions. In Figure 4, we show that there is a significant offset between the observed temperature profile and that expected for a cluster in hydrostatic equilibrium. This is further illustrated in Figure 5 where we compare the fractional difference between hydrostatic equilibrium masses and the true masses for our simulated clusters. Here, we find that this fractional difference becomes larger in going from the cluster core to the virial radius (biased low by an average of ≈15% with significant scatter).

We pursued the origin of the difference between hydrostatic and true masses at the cluster peripheries by examining the energy density ratios for our numerical cluster sample. That is, we compared the thermal, radial kinetic, and turbulent kinetic energy densities as a function of radial distance. At radii of ≲$0.2r_{200}$, the radial kinetic and turbulent kinetic energies contribute ≈15% to the total nongravitational energy of the ICM. However, near the virial radius, the radial kinetic energy equals the thermal energy, and the turbulent kinetic energy is about 50% of the thermal energy. So, there is significant nonthermal pressure support of the gas in the outer ICM where the clusters connect to filaments which channel fresh gas into the clusters. We believe that these turbulent gas motions are a major source of the disagreement between hydrostatic and true masses in the outer parts of clusters.

In conclusion, the new *Suzaku* temperature profiles, which extend out to ≈r_{200}, offer important insights into the nature of gas at galaxy cluster peripheries. On the one hand, the thermodynamics is simple and well modeled by adiabatic gas physics since cooling times are long and other nongravitational physics (e.g., AGN heating, cosmic rays) seems negligible. On the other hand, the gas dynamics is complex at the intersection of cosmic web filaments where galaxy clusters live. This is further illustrated in Figure 6. Turbulent gas motions are likely the source of bias between hydrostatic and true cluster masses.

REFERENCES

Allen, S. W., Rapetti, D. A., Schmidt, R. W., Ebeling, H., Morris, R. G., & Fabian, A. C. 2008, MNRAS, 383, 879
Bautz, M. W., et al. 2009, PASJ, 61, 1117
Borgani, S., & Kravtsov, A. 2009, arXiv:0906.4370
Bryan, G. L., & Norman, M. L. 1997a, in ASP Conf. Ser. 123, 12th Kingston Meeting on Theoretical Astrophysics, Halifax, Nova Scotia, Canada, 1996 October 17–19, ed. D. A. Clarke & M. J. West (San Francisco, CA: ASP), 363
Bryan, G. L., & Norman, M. L. 1997b, in Workshop on Structured Adaptive Mesh Refinement Grid Methods, ed. N. Chrisochoides (IMA Volumes in Mathematics, 117; New York: Springer-Verlag), 433
Burns, J. O. 1998, Science, 280, 400
Burns, J. O., Hallman, E. J., Gantner, B., Motl, P. M., & Norman, M. L. 2008, ApJ, 675, 1125
Churazov, E., Forman, W., Vikhlinin, A., Tremaine, S., Gerhard, O., & Jones, C. 2008, MNRAS, 388, 1062
De Grandi, S., & Molendi, S. 2002, ApJ, 567, 163
Eisenstein, D. J., & Hu, W. 1999, ApJ, 511, 5
Eisenstein, D. J., & Hut, P. 1998, ApJ, 498, 137
Eke, V. R., Navarro, J. F., & Frenk, C. S. 1998, ApJ, 503, 569
Fabjan, D., Borgani, S., Tornatore, L., Saro, A., Murante, G., & Dolag, K. 2010, MNRAS, 401, 1670
Ferland, G. J., Korista, K. T., Verner, D. A., Ferguson, J. W., Kingdon, J. B., & Verner, E. M. 1998, PASP, 110, 761
Fujita, Y., Tawa, N., Hayashida, K., Takizawa, M., Matsumoto, H., Okabe, N., & Reiprich, T. H. 2008, PASJ, 60, 343
George, M. R., Fabian, A. C., Sanders, J. S., Young, A. J., & Russell, H. R. 2009, MNRAS, 395, 657
Hart, Q. N., Stocke, J. T., & Hallman, E. J. 2009, ApJ, 705, 854

Heinz, S., Reynolds, C. S., & Begelman, M. C. 1998, ApJ, 501, 126
Henry, J. P., Evrard, A. E., Hoekstra, H., Babul, A., & Mahdavi, A. 2009, ApJ, 691, 1307
Hoshino, A., et al. 2010, PASJ, 62, 371
Jeltema, T. E., Hallman, E. J., Burns, J. O., & Motl, P. M. 2008, ApJ, 681, 167
Kawaharada, M., et al. 2010, ApJ, 714, 423
Lau, E. T., Kravtsov, A. V., & Nagai, D. 2009, ApJ, 705, 1129
Loken, C., Norman, M. L., Nelson, E., Burns, J., Bryan, G. L., & Motl, P. 2002, ApJ, 579, 571
Lovisari, L., Kapferer, W., Schindler, S., & Ferrari, C. 2009, A&A, 508, 191
Mahdavi, A., Hoekstra, H., Babul, A., & Henry, J. P. 2008, MNRAS, 384, 1567
Mantz, A., Allen, S. W., Ebeling, H., Rapetti, D., & Drlica-Wagner, A. 2010, MNRAS, 406, 1773
Meneghetti, M., Rasia, E., Merten, J., Bellagamba, F., Ettori, S., Mazzotta, P., Dolag, K., & Marri, S. 2010, A&A, 514, A93
Motl, P. M., Hallman, E. J., Burns, J. O., & Norman, M. L. 2005, ApJ, 623, L63
Nagai, D. 2006, ApJ, 650, 538
Nagai, D., Vikhlinin, A., & Kravtsov, A. V. 2007, ApJ, 655, 98
Norman, M. L., & Bryan, G. L. 1999, in Numerical Astrophysicsin Proc. International Conference on Numerical Astrophysics 1998, Numerical Astrophysics, ed. S. M. Miyama, K. Tomisaka, & T. Hanawa (Boston, MA: Kluwer), 19
Oguri, M., Takada, M., Okabe, N., & Smith, G. P. 2010, MNRAS, 405, 2215
O'Shea, B. W., Bryan, G. L., Bordner, J., Norman, M. L., Abel, T., Harkness, R., & Kritsuk, A. 2004, in Adaptive Mesh Refinement–Theory and Applications, 3044, ed. T. Plewa, T. J. Linde, & V. G. Weirs (New York: Springer), 341
O'Shea, B. W., Nagamine, K., Springel, V., Hernquist, L., & Norman, M. L. 2005, ApJS, 160, 1
Piffaretti, R., & Valdarnini, R. 2008, A&A, 491, 71
Rapetti, D., Allen, S. W., & Mantz, A. 2008, MNRAS, 388, 1265
Rasia, E., et al. 2006, MNRAS, 369, 2013
Reiprich, T. H., et al. 2009, A&A, 501, 899
Roncarelli, M., Ettori, S., Dolag, K., Moscardini, L., Borgani, S., & Murante, G. 2006, MNRAS, 373, 1339
Rosati, P., Borgani, S., & Norman, C. 2002, ARA&A, 40, 539
Ruszkowski, M., & Begelman, M. C. 2002, ApJ, 581, 223
Skillman, S. W., Hallman, E. J., O'Shea, B. W., Burns, J. O., Smith, B. D., & Turk, M. J. 2010, arXiv:1006.3559
Skillman, S. W., O'Shea, B. W., Hallman, E. J., Burns, J. O., & Norman, M. L. 2008, ApJ, 689, 1063
Smith, B., Sigurdsson, S., & Abel, T. 2008, MNRAS, 385, 1443
Spergel, D. N., et al. 2007, ApJS, 170, 377
Stone, J. M., & Norman, M. L. 1992a, ApJS, 80, 753
Stone, J. M., & Norman, M. L. 1992b, ApJS, 80, 791
Tornatore, L., Borgani, S., Viel, M., & Springel, V. 2010, MNRAS, 402, 1911
Vazza, F., Brunetti, G., Kritsuk, A., Wagner, R., Gheller, C., & Norman, M. 2009, A&A, 504, 33
Vikhlinin, A., Kravtsov, A., Forman, W., Jones, C., Markevitch, M., Murray, S. S., & Van Speybroeck, L. 2006, ApJ, 640, 691
Vikhlinin, A., et al. 2009, ApJ, 692, 1060
Voit, G. M. 2005, Rev. Mod. Phys., 77, 207
Xu, H., Li, H., Collins, D. C., Li, S., & Norman, M. L. 2009, ApJ, 698, L14